LITHOS 518-519 (2025) 108326

Contents lists available at ScienceDirect

LITHOS

journal homepage: www.elsevier.com/locate/lithos

Polyphase polygonal serpentine veins in the Rocciavrè meta-ophiolite (Western Alps, NW Italy)

Luca Barale [a,b], Giancarlo Capitani [c,*], Roberto Compagnoni [b,d], Roberto Conconi [e], Roberto Cossio [b,d], Linda Pastero [d], Marcello Mellini [b]

[a] Institute of Geosciences and Earth Resources, National Research Council of Italy, Via Valperga Caluso 35, 10125 Turin, Italy
[b] "G. Scansetti" Interdepartmental Center for Studies on Asbestos and Other Toxic Particulates, University of Turin, Via Pietro Giuria 7, 10125 Turin, Italy
[c] Department of Earth and Environmental Sciences, University of Milano-Bicocca, Piazza della Scienza 4, 20126 Milan, Italy
[d] Department of Earth Sciences, University of Turin, Via Valperga Caluso 35, 10125 Turin, Italy
[e] Unité Matériaux et Transformations, Université de Lille, Cité Scientifique bâtiment C6, Villeneuve d'Ascq, 59655 Lille, France

ARTICLE INFO

Keywords:
Polygonal serpentine
Al-lizardite porphyroblasts
Metadunite-vein reaction zone

ABSTRACT

Widespread polygonal serpentine (PS) veins occur in the ultramafics of the Rocciavrè meta-ophiolite, which consists of alternating metadunite and antigorite-serpentinite bands. The PS veins exhibit a complex polyphasic history that includes three PS domains (Dom 1, Dom 2 and Dom 3), porphyroblasts of aluminian-lizardite (Al-Lz) and minor brucite. Four steps of vein dilation have been recognized. The microstructure indicates that Dom 1 is constituted by a PS pseudomorph after the original olivine, the first mineral that heterogeneously nucleated on the fracture wall. Al-Lz and brucite porphyroblasts developed near the wall-rock overgrowing olivine. Dom 2 is constituted by an aggregate of PS + brucite that completely seals the vein. Dom 3 is constituted by the last generation of PS that grew as coarser-grained fiber bundles partially replacing Dom 2.

Chemical analyses showed that PS of Dom 1 and Dom 2 have a similar, very low Fe-content, whereas PS of Dom 3 have systematically slightly higher Fe, which is possibly responsible for the rusty color typical of weathered surfaces. Porphyroblastic Al-Lz has high Al and minor Fe contents. Late barite sealed fractures opened in correspondence of Al-Lz cleavage planes. X-ray powder diffraction and μ-Raman revealed the presence of both PS polytypes, PS-15, with 15 sectors, and PS-30, with 30 sectors, respectively, and minor brucite. TEM images showed the presence of both PS-15 and PS-30, locally associated with brucite and rare chrysotile. μ-Raman maps confirmed that all domains contain the same submicroscopic association of PS-15, PS-30 and brucite, in highly variable ratios from point to point.

Each PS vein is bounded by two reaction zones, where the host metadunite is altered to an aggregate of lizardite + magnetite + brucite + minor chlorite with accessory awaruite and heazlewoodite. Therefore, the close relationship between metadunite and PS veins supports a local origin for vein feeding elements. The vein mineralogy indicates genetic conditions characterized by CO_2-free aqueous fluid, slightly silica-undersaturated bulk composition, and low f_{O2} compatible with magnetite, Fe=Ni alloys and Ni sulphides. The PS veins are crossed by later chrysotile veinlets, in turn cut by very thin veins of euhedral brucite included in a fine-grained carbonate aggregate, identified by μ-Raman spectroscopy as a mixture of artinite and hydromagnesite.

The coeval development of PS in the vein and lizardite in the reaction zone of the host metadunite suggests that these two phases must have, at least in part, a superposed stability field and that other factors, including kinetics factors, must be responsible for the fibrous habit of serpentine – either chrysotile or PS, since the latter derives from the former – in the vein.

1. Introduction

Polygonal serpentine (e.g., Baronnet and Devouard, 2005; Enju et al., 2023; Mugnaioli et al., 2007), is a member of the serpentine group, i.e. 1:1 phyllosilicates with ideal composition of $Mg_3Si_2O_5(OH)_4$. Other relevant members of the group are: antigorite (Capitani and Mellini,

* Corresponding author.
E-mail address: giancarlo.capitani@unimib.it (G. Capitani).

https://doi.org/10.1016/j.lithos.2025.108326
Received 23 May 2025; Received in revised form 23 October 2025; Accepted 1 November 2025
Available online 13 November 2025

2004, 2006), lizardite (e.g., Brigatti et al., 1997; Mellini, 1982), chrysotile (e.g., Enju et al., 2023; Whittaker and Zussman, 1956) and polyhedral serpentine (e.g., Baronnet et al., 2007; Cressey et al., 2008). Serpentine minerals are composed of a hexagonal array of corner-sharing SiO_4 tetrahedra and a trioctahedral sheet of edge-sharing Mg-(O,OH) octahedra. The sheets are linked by sharing apical oxygens, and each layer is joined by weak hydrogen bonds. Antigorite, lizardite, and chrysotile are made up of repeats of wavy, flat, and cylindrically curved layers, respectively. Polygonal and polyhedral serpentine include fragments of structures of both lizardite and chrysotile (Baronnet et al., 2007; Baronnet and Devouard, 2005; Mugnaioli et al., 2007). In most cases, several serpentine group minerals occur together in the same rock, testifying their very close stability field and/or growing conditions driven by kinetics factors.

Polygonal serpentine (PS) was first regarded as a unique variant of chrysotile, called "splintery chrysotile" or "Povlen-type chrysotile", due to the similarity in form, occurrence, and crystallographic features. Later, with the advent of TEM techniques, the polygonal structure was directly observed and then disentangled (e.g., Baronnet and Devouard, 2005; Mellini, 1986; Mugnaioli et al., 2007). These observations converged in sustaining the model by Baronnet et al. (1994), wherein the layers are continuous among sectors with curvature at sector boundaries, by shifting of the adjacent stacking layers. So far, two main PS variants have been reported, PS-15 and PS-30, made of fifteen and thirty sectors, rotated each other by 24 or 12°, respectively (e.g., Barale et al., 2023; Mugnaioli et al., 2007). While the basic crystallographic properties of PS have been established by these previous studies, their variation, occurrence, and formation conditions are still poorly understood.

As part of a research project aimed at studying mineral veins in serpentinites of the Western Alps, a new type of vein characterized by polygonal serpentine was discovered in Monte Avic Massif in Aosta Valley (Barale et al., 2023). In this paper, we are dealing with the outcomes of a new field survey in the Orsiera-Rocciavrè Massif, which has revealed in ultramafics the common occurrence of networks of serpentine veins very similar to those studied at Monte Avic, but structurally more complex. The systematic study of the numerous samples collected has shown that they are polyphasic veins formed at different times, but characterized by a similar mineral assemblage including PS (PS-15 and PS-30) and brucite.

The widespread occurrence of these polyphase veins in the Rocciavrè Massif has allowed us to better understand their emplacement mechanisms. Thus, PS-15 and PS-30 are no longer to be considered as mineralogical oddities, but rather serpentine phases that grow in late metamorphic veins of peculiar geological contexts, where influxes of aqueous fluids, possibly derived from the antigorite breakdown, are reacting with the olivine of metadunite.

Therefore, PS veins are expected to be much more common in nature, provided that ophiolitic massifs such as Rocciavrè and Monte Avic, which experienced prograde high-pressure (HP) eclogite-facies metamorphism, are studied in detail using suitable techniques such as High Resolution Transmission Electron Microscopy (HR-TEM) and μ-Raman Spectroscopy.

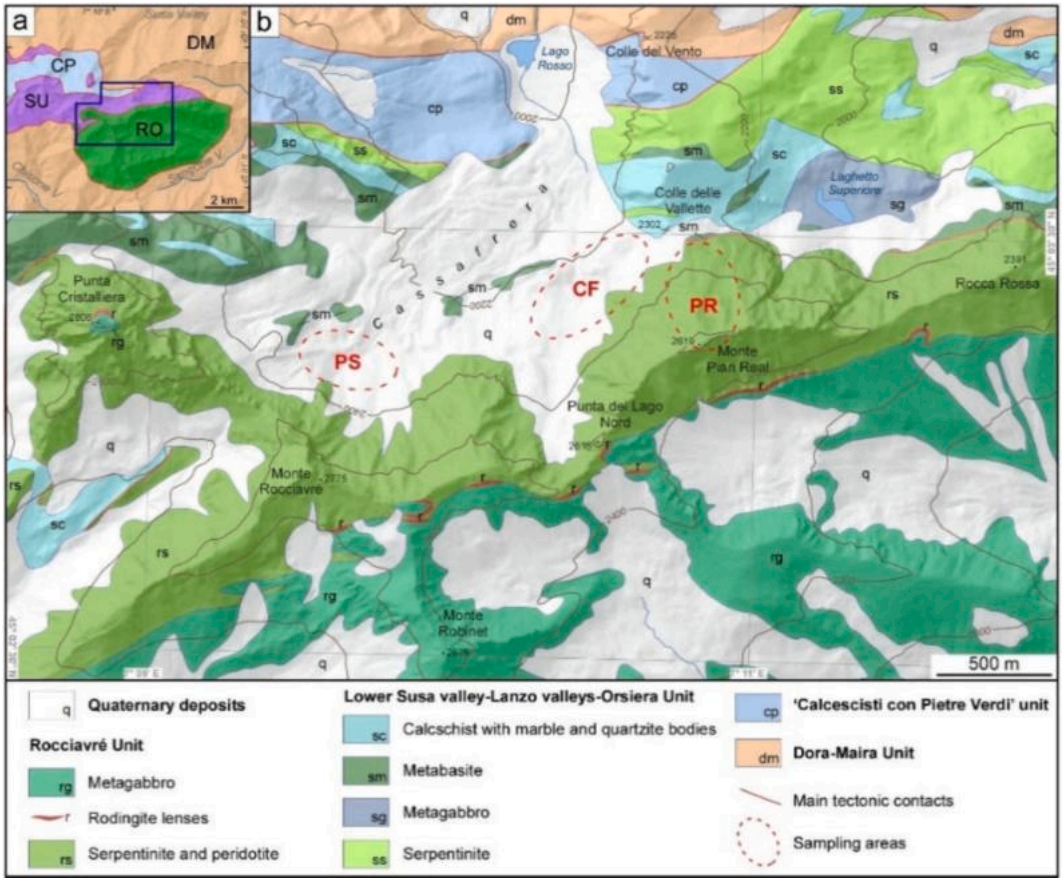

Fig. 1. **a**: Orsiera-Rocciavrè Klippe of meta-ophiolite and calc-schists, overlying the continental Dora-Maira Massif (DM). The Klippe is exposed on the divide between the Susa Valley to the North, Val Chisone to SW and Val Sangone to SE. RO: Rocciavrè Unit; SU: Lower Susa Valley – Lanzo Valleys - Orsiera Unit; CP: 'Calcescisti con Pietre Verdi' (Calc-schists with meta-ophiolite) unit (after Cadoppi et al., 2002). **b**: Geolithological map of the examined area (after Pognante, 1979 and Cadoppi et al., 2002, modified). The vein sampling areas are shown by red dashed ellipses: PS: Western Cassafrera depression; CF: Eastern Cassafrera depression; PR: Monte Pian Real.

2. Geological outlines of the Orsiera-Rocciavrè Klippe

The Orsiera-Rocciavrè meta-ophiolite is a Klippe exposed on the divide between Val di Susa to the north and Val Chisone to the south, on the Italian side of the Cottian Alps (Fig. 1). The Klippe belongs to the internal part of the "Piemonte Zone of Calc-schists with meta-ophiolites", which is characterized by an Alpine eclogite-facies metamorphic overprint (e.g., Piana et al., 2017, with refs. therein). It overlies the continental crust of the Dora-Maira Massif, which is also overprinted by Alpine eclogite-facies metamorphism (Fig. 1).

In the Orsiera-Rocciavrè Klippe, the Rocciavrè portion mainly consists of eclogite-facies metagabbro and ultramafics with negligible metasediments (Pognante, 1979, 1985). The top of the ridge, from Punta Cristalliera to the west to Rocca Rossa to the east, is made of ultramafic rocks that are extensively exposed on the northern slope and cliffs (Fig. 1 **b**). The ultramafics are juxtaposed to eclogite-facies metagabbros and the contact is marked by an alignment of rodingite boudins.

Among the most recent papers focused on the Rocciavrè Massif, Herviou et al. (2025) report an exhaustive study on the metamorphic veins of eclogites, which allows a precise characterization of the fluid–rock interaction processes during subduction from the pressure peak to the exhumation at greenschist-facies conditions.

3. Experimental methods

The rocks were studied in polished thin sections by optical microscopy and microanalysis. Chemical data were acquired with a Scanning Electron Microscope (SEM) JEOL JSM-IT300LV, equipped with Energy Dispersive Spectrometer (EDS) Oxford Instruments X-act silicon drift detector. Operating conditions were: E = 15 keV, working distance = 10 mm, magnification = 50× (2.55 × 1.9 mm scanned area), 1024 × 768 pixels (res = 2.5 μm), probe current = 5 nA, process time = 1 μs (10^5 counts per second (CPS) with a dead time of 30 %), SmartMap dwell time = 10 ms. Phase maps were obtained with AZtec AutoPhaseMap (Oxford Instruments) from quantitative X-ray maps of individual elements calculated with AZtec QuantMap (Oxford Instruments). Sum spectra extracted for each main phase (Lz: lizardite, Spl: spinel, Mag: magnetite) were quantitatively corrected using the ZAF procedure. Atom concentrations per formula unit (a.p.f.u) were obtained by means of Lanari functions (Lanari et al., 2014).

The X-ray Powder Diffraction (XRPD) patterns were performed with a Rigaku Smartlab XE Bragg-Brentano diffractometer equipped with Ni-filtered Cukα radiation and an X-ray tube operating at 40 kV and 30 mA. XRPD patterns were collected in the range $5° < 2\theta < 85°$ with 0.01° steps, using a θ/2θ geometry and a HyPix3000 area detector. The scanning rate for micro-area (2 mm × 1 mm) measurements on polished rock slabs was 0.1°/min, whereas for experiments with grinded samples, loaded on Si zero-background sample-holder, was 0.5°/min. X-ray diffraction data were processed using Match! v.4.1 (2025) software (https://www.crystalimpact.de/match), the Crystallography Open Database (COD), and Fityk v.0.9.8 software for pattern deconvolution (Wojdyr, 2010).

Transmission Electron Microscopy (TEM) data were acquired at the Platform of Microscopy of the University of Milano-Bicocca (PMiB) with a JEOL JEM 2100P, operated at 200 kV and equipped with an Oxford EDS system for elemental analysis and a 3 k × 3 k Gatan Rio CMOS camera for image acquisition. EDS analyses were collected in STEM (scanning) mode and quantified using the Cliff-Lorimer approximation (Conconi et al., 2023). Samples were prepared at the PMiB by ion milling 3 mm wide disks selected on a double polished petrographic thin section using a Gatan PIPS-II instrument. To minimize beam damage during ion milling, the sample holder was cooled with liquid nitrogen. TEM-mounts were coated with 5 nm of graphite to avoid electrostatic charging during observations.

μ-Raman measurements were carried out with a green laser (532 nm) and a 100× objective. Only the high-wavelength region between 2600 and 3750 cm^{-1} was considered in detail, because including the most informative part of the spectrum, characterized by peaks arising from the hydroxyl stretching modes. To obtain more information on the relative abundances of the three submicroscopic mineral phases identified by TEM (PS-15, PS-30, brucite), a high number of μ-Raman randomly selected spot analyses were performed in two different veins. Given the variability of the results, due to the extremely fine grain-size of the minerals, as evident from the TEM data, we proceeded to analyze statistically more representative μ-Raman maps (App. 1, Fig. S1). Each spectrum was acquired with two repetitions of one second. The background was subtracted using a 2nd degree polynomial. A reliable peak deconvolution was performed with a voigtian fitting of 6 bands. Spectra were processed using the net area of each peak (App. 1, Fig. S2). Each map scanned an area of ~1 mm^2 (30 × 30 μm) with steps of 1 μm, for a total of ~960 single spectra (App. 1, Fig. S3). μ-Raman maps were carried out on three domains (Dom 1, Dom 2, Dom 3, see below), randomly selected from three different veins (labelled PS06b, PS07 and PS10), for a total of more than 8500 spectra. The interpretation of the Raman spectra was carried out taking into consideration the peak shifts related to the anisotropy of each mineral of the serpentine family, as shown by Compagnoni et al. (2021) and detailed in Appendix 1.

4. Results

4.1. Petrography

Metadunite, the vein-hosting rock. A re-examination of the entire northern slope of the ridge between Punta Cristalliera and Monte Pian Real showed that the ultramafic rocks are made up of plurimetric to pluridecametric alternating bands, reddish or greenish on weathered surface, and corresponding to metadunite and antigorite serpentinite, respectively. Only metadunites host the PS veins. Samples were collected along the northern wall of the ridge and in the Quaternary deposits lying at its feet, in three areas marked by the acronyms PS, CF and PR (Fig. 1 **b**). Metadunite consists of forsterite, antigorite, magnetite, Mg-chlorite and titanian hydroxylclinohumite, that is the typical assemblage of the Alpine eclogite-facies metamorphism in the ultramafics of Western Alps. The ultramafic rocks show an evident polyphase mylonitic fabric (App. 2, Fig. S1 **a**), where antigorite progressively transforms to forsterite. These relationships suggest that the alternation of the two lithologies results from the fluids released by advanced (metadunite) or incipient (serpentinite) degree of antigorite to forsterite transformation. Olivine has a high forsterite content (~Fo_{88}) and occurs as blasts strongly elongated parallel to mylonitic foliation that are in equilibrium with magnetite and titanian hydroxylclinohumite.

Polygonal serpentine veins. PS veins form an irregular network of greenish anastomosing branches, from few mm to several cm thick, widely variable in continuity, thickness and orientation (App. 2, Figs. S2 **a** and **b**). As evident from Fig. 2, the internal structure of the veins is roughly symmetrical and consists of three main domains, labelled Dom 1, Dom 2 and Dom 3. Dom 1 occurs on both vein selvages; Dom 2 constitutes the main central part of the vein; Dom 3 grows discontinuously from the vein selvages towards the center. On both selvages of the vein, Al-lizardite and minor brucite porphyroblasts locally grew inward (Figs. 2 **a** to **d**). Microstructural relationships indicate that Dom 1, Dom 2 and Dom 3 grew in chronological order. Al-lizardite developed early in the vein history, but after the former olivine of Dom 1.

Porphyroblasts. Porphyroblasts of lizardite and brucite, almost black on the hand specimen (Fig. 2 **e**) and highlighted in green in Figs. 2 **b** and **d**, are colorless in thin section under plane polarized light (PPL), with low birefringence under crossed polarizers light (XP) (Figs. 2 **g** and 4 **b**). Porphyroblasts normally occur close to the vein selvages as crystals a few mm across (Figs. 2 **a** to **g**) with characteristic "butterfly" habit (Figs. 3 and 4 **a**, **b**). The size and "butterfly" habit of Al-Lz suggest a fast growth in a hydrous fluid medium. Al-Lz, slightly deformed and corroded by Dom 2 and 3 (Figs. 3 **a** and **b**), appears to have grown later

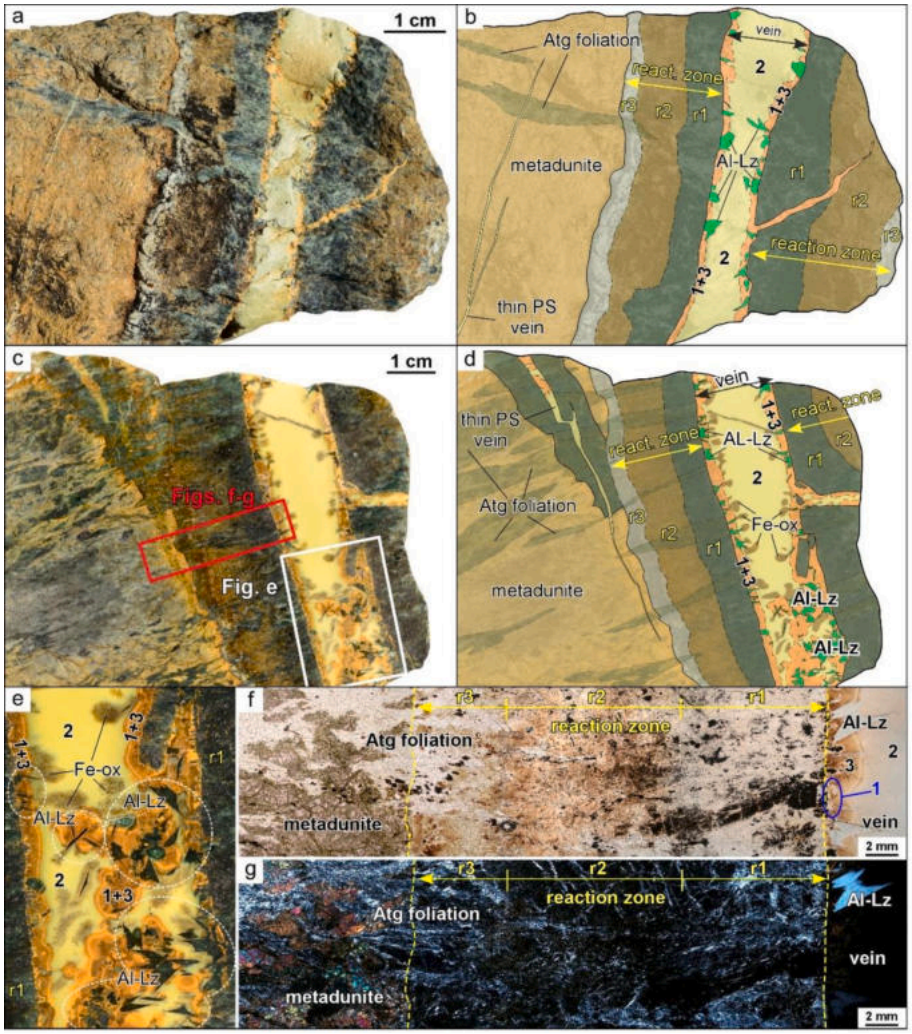

Fig. 2. Sample CF04. **a** to **d**: Representative images of two PS veins cutting across the host metadunite. Contacts are altered by a reaction zone, few mm to several cm thick, especially evident on the weathered surface (**a** and **b**) and on the polished slab (**c** and **d**). The veins are polyphasic and consist of three stages of polygonal serpentine emplacement, labelled in chronological order 1 (Dom 1), 2 (Dom 2), and 3 (Dom 3), together with Al-rich lizardite porphyroblasts (Al-Lz) and minor brucite (Brc). Three layers, labelled r1, r2 and r3, have been distinguished in the reaction zone (**a**, **b** and **c**, **d**). In sketches **b** and **d**, Al-Lz is highlighted in green; **e**) Enlarged portion of image **c** included in the white inset: the brownish portions, labelled 1 + 3, are Dom 3 overgrowing and replacing Dom 2. On the surface of the polished sample, Al-Lz appears dark. **f**) and **g**): Photomicrograph of the red inset in image **c** that includes the whole reaction zone from the fresh metadunite (left) to the PS vein (right), in which an Al-Lz porphyroblast occurs with characteristic "butterfly" habit; **f**: PPL (Plane Polarized Light), **g**: XP (crossed polarizers). (For interpretation of the references to color in this figure legend, the reader is referred to the web version of this article.)

than Dom 1 (Figs. 3 **a**, **b** and 5 **a**, **b**).

Domain 1. Dom 1 occurs just at the contact with the host metadunite as chains of roundish bodies, a few tens of micrometers to several millimeters across. On the hand specimen, Dom 1 appears greenish (App. 2, Figs. S2 **a**, **b**) to yellowish in color (Figs. 2 **a, c**, **e**). In the thin section, Dom 1 is colorless and homogeneous under PPL (Figs. 4 **a**, **c**), with dark grey interference colors under XP and complex heterogeneous extinction (Fig. 5 **b**). Since their contours normally have polygonal shape (Figs. 4 **a**, **c**), these domains have been interpreted as pseudomorphs after a former mineral, most likely forsterite, although not identified with certainty. Dom 1 may include small magnetite crystals; locally, it is also overgrown by large magnetite aggregates (Fig. 3 **a**).

Domain 2. Dom 2, which constitutes the central main portion of each vein, is pale yellowish on the hand specimen (Figs. 2 **a** to **e**) and very pale pinkish and optically homogeneous (Figs. 4 **a**, **c**) with very low birefringence in thin section (Figs. 4 **b**, **d**). Normally, the PS fibers cannot be resolved under the optical microscope even at high magnification.

Domain 3. Dom 3 has a greenish or orange to red-brownish color on the hand specimen (Fig. 2) and from dark brown (Fig. 4 **a**) to light brown (Fig. 4 **c**) in thin section, with color depth varying from sample to sample. The brownish color most likely depends on the oxidation degree of Fe, whose content is normally higher than in the other two domains (Table 1). Dom 3 occurs as discontinuous layers at the vein selvages that envelope Dom 1 (Figs. 4 **a** to **d**). Unlike the other domains, Dom 3 exhibits the fibrous microstructure of PS (Fig. 4 c), which is characterized by radiating bundles of fibrils (Fig. 5 **b**) growing from the host rock inward by replacing and/or overgrowing Dom 2 (Figs. 3 **a**, **b** and 4 **a**, **c**).

Opaque ores. The ubiquitous opaque mineral is magnetite, which occurs as irregular grains and grain aggregates mostly concentrated at the vein - reaction zone contact (Figs. 4 **c**, 5 **a** and App. 3, Figs. S1, BSE image and Fe map). In the reaction zone, tiny accessory grains of Ni-bearing ores locally occur and have been identified by X-ray maps as awaruite and heazlewoodite (App. 3, Fig. S1, Ni map). Both minerals have been reported by Manavella et al. (2021) from a "serpentine" (actually PS) vein of the same locality.

Latest veins. Thin veinlets cross-cutting the PS veins are filled with chrysotile (App. 2, Figs. S2 a and S3 **a**, **b**). In one case, a chrysotile vein

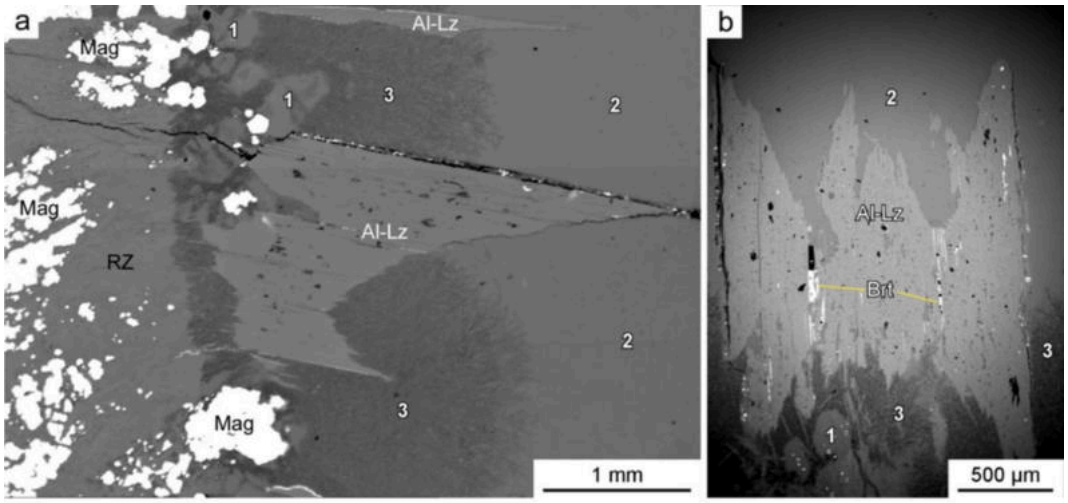

Fig. 3. Sample CF04. **a**: BSE image of the contact between the vein (right) and the reaction zone (RZ) derived from the alteration of the host metadunite (left). Microstructural relationships indicate that Al-Lz is an earlier phase being corroded by PS of Dom 2 (2) and Dom 3 (3). **b**: BSE image of another Al-Lz porphyroblast close to the host metadunite contact (on the right, outside the picture), which is strongly corroded by PS of Dom 2 (2) and Dom 3 (3). Some (001) cleavage planes of Al-Lz have been filled with barite (Brt).

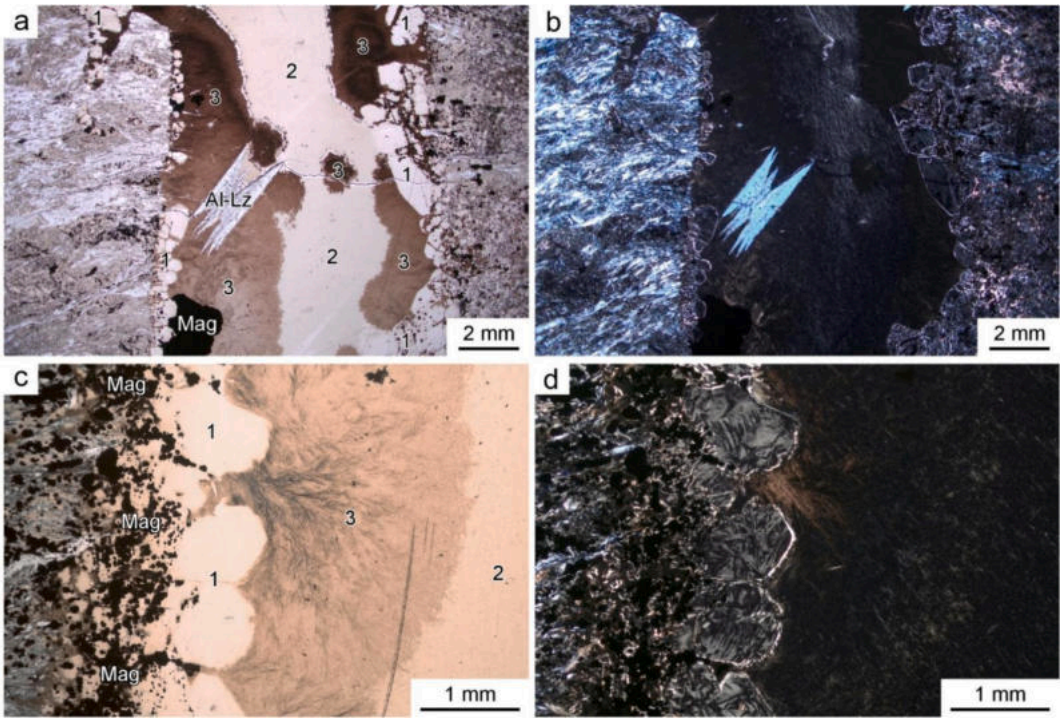

Fig. 4. Sample PS06b. Photomicrographs of PS veins with evident microstructural relationships among Dom 1 (1), Dom 2 (2), Dom 3 (3), magnetite (Mag), and Al-lizardite (Al-Lz) porphyroblasts. **a, b**: On both sides of the vein, the host metadunite is retrogressed to lizardite + magnetite ± brucite. **c, d**: Details of Domains 1 that exhibit a "euhedral" habit and a complex microstructure at XP. Note the variable brownish color depths of Dom 3 and its evident fibrous microstructure and Mag concentration at the vein-metadunite contact. PPL: left; XP: right.

was cut by a subparallel veinlet consisting of euhedral brucite and fine-grained carbonate aggregates (App. 2, Fig. S3). Carbonate was identified by μ-Raman spectroscopy as a mixture of artinite [$Mg_2(CO_3)(OH)_2{\cdot}3(H_2O)$] and hydromagnesite [$Mg_5(CO_3)_4(OH)_2{\cdot}4H_2O$] (App. 2, Figs. S3 **a**, **b**).

4.2. Mineral chemistry

Domains 1, 2, 3 and Al-lizardite porphyroblasts. Dom 1 (Table 1, column E) and Dom 2 (Table 1, columns D and F) have similar compositions and essentially consist of Mg and Si with minor Fe (FeO = 2.4–2.6 wt%). These data are consistent with the composition of a homogeneous serpentine, as suggested by low standard deviations and closeness to five atoms per formula unit (based on 7 anhydrous oxygens). The analyses performed in Dom 3 are less homogeneous, and at least two different situations can be distinguished: i) in the first case (column G), despite the apparent homogeneity under optical microscopy, Mg is too high and Si too low for the presence of just one serpentine mineral. Furthermore, the standard deviations of Mg and Si are unusually high, and the total cation sum always greater than 5.0 a.p.f.u. These features indicate that

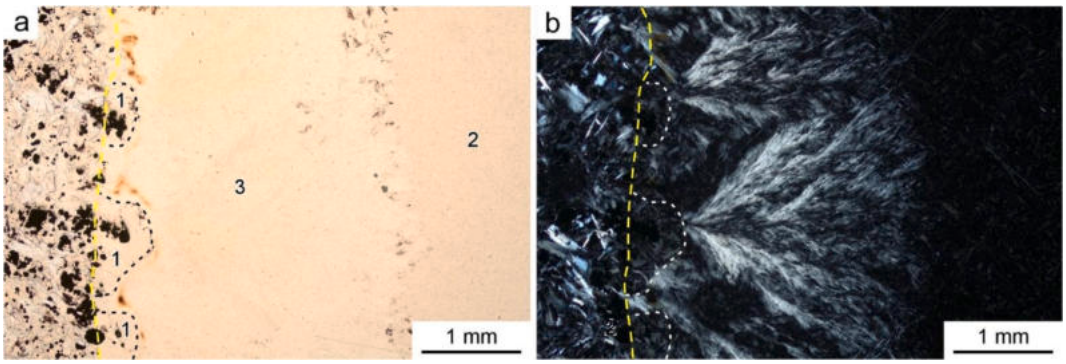

Fig. 5. Sample CF03. Photomicrographs **a** (PPL) and **b** (XP) of the three domains with radiating arrays of coarser-grained PS fiber bundles in Dom 3, growing from the host metadunite contact towards the inner portion of the vein and replacing Dom 2.

Table 1
Mean oxide (wt%) chemical compositions (standard deviation every second column) and atoms per formula unit (a.p.f.u.) of serpentines representative of Domains 1, 2, 3 and Al-lizardite (Sample PS001).

	Site 1								Site 2							
	A		B		C		D		E		F		G		H	
Label (N° of anal.)	Dom3-Mat. (12)		Dom3-Fib. (13)		Al-Lz (73)		Dom2 (16)		Dom1 (9)		Dom2 (8)		Dom3 (9)		Al-Lz (12)	
MgO	40.76	0.08	39.85	0.09	35.77	0.39	41.18	0.16	41.16	0.52	40.94	0.36	43.19	3.75	36.22	0.31
Al_2O_3	0.16	0.10	0.11	0.03	8.55	0.56	0.09	0.06	b.d.l.	–	0.04	0.06	0.04	0.04	9.20	1.61
SiO_2	42.89	0.12	42.01	0.13	35.76	0.35	43.45	0.07	43.55	0.33	43.54	0.27	39.34	3.30	37.10	1.59
Cr_2O_3	0.01	0.02	b.d.l.	–	3.08	0.28	0.01	0.03	b.d.l.	–	b.d.l.	–	b.d.l.	–	0.22	0.37
MnO	0.09	0.05	0.24	0.03	0.01	0.05	0.03	0.04	0.03	0.04	0.05	0.05	0.19	0.14	b.d.l.	–
FeO	3.31	0.21	5.00	0.18	3.84	0.20	2.48	0.12	2.39	0.21	2.56	0.07	4.29	0.28	4.57	0.23
NiO	b.d.l.	–	b.d.l.	–	0.21	0.11	b.d.l.	–	b.d.l.	–	b.d.l.	–	0.16	0.16	b.d.l.	–
Σ	87.22		87.19		87.22		87.25		87.57		87.14		87.21		87.31	
								a.p.f.u.								
Si_T	2.005	0.003	1.987	0.004	1.703	0.016	2.020	0.003	2.028	0.015	2.030	0.011	1.866	0.143	1.748	0.068
Al_T	0.000	0.000	0.013	0.004	0.297	0.016	0.000	0.000	b.d.l.	–	0.003	0.005	0.001	0.003	0.250	0.050
Fe_M	0.130	0.008	0.198	0.007	0.153	0.008	0.096	0.005	0.094	0.007	0.100	0.000	0.170	0.011	0.181	0.010
Mg_M	2.842	0.005	2.810	0.005	2.540	0.026	2.855	0.010	2.856	0.037	2.843	0.027	3.059	0.288	2.544	0.017
Cr_M	0.000	0.001	b.d.l.	–	0.116	0.011	0.000	0.001	b.d.l.	–	b.d.l.	–	b.d.l.	–	0.008	0.014
Ni_M	b.d.l.	–	b.d.l.	–	0.008	0.004	b.d.l.	–	b.d.l.	–	b.d.l.	–	0.006	0.005	b.d.l.	–
Al_M	0.009	0.005	0.000	0.001	0.183	0.019	0.005	0.003	b.d.l.	–	0.000	0.000	0.000	0.000	0.260	0.050
Mn_M	0.004	0.002	0.009	0.001	0.000	0.002	0.001	0.002	0.000	0.000	0.001	0.004	0.008	0.007	b.d.l.	–
Σ_{Cat}	4.990	0.005	5.018	0.008	4.999	0.008	4.977	0.003	4.978	0.005	4.976	0.006	5.109	0.045	4.991	0.006
X_{Fe}	0.044	0.003	0.066	0.002	0.054	0.003	0.033	0.002	0.032	0.003	0.034	0.003	0.053	0.002	0.066	0.002
X_{Mg}	0.956	0.003	0.934	0.002	0.902	0.005	0.967	0.002	0.968	0.003	0.966	0.003	0.947	0.002	0.934	0.002

b.d.l. = below detection limit.

Dom 3 is a submicroscopic intergrowth of PS and brucite, as confirmed by TEM (see Sections 4.4) and μ-Raman (see Sections 4.5); ii) in the second case, which under optical microscopy appears to consist of fiber bundles included in a seemingly homogeneous matrix (Fig. 5), the matrix (column A) has a composition very similar to that of Dom 2 with a slightly higher Fe content (FeO = 3.31 wt%). The fiber bundles (Table 1, column B) show even higher Fe (FeO = 5.00 wt%) and small but constant Mn (MnO = 0.24 wt%) contents. Since the cation sum is close to 5, we assume that this is the real composition of the fiber bundles in Dom 3. This higher Fe content probably contributes to the systematic "rusty" color of the weathered surface of Dom 3. Whereas brucite porphyroblasts have normal stoichiometric composition, Al-Lz porphyroblasts have Al_2O_3 content ~9.00 wt% (slightly lower in column C and slightly higher in column H), relatively high FeO content ranging from 3.84 wt% (column C) to 4.57 wt% (column H), and in one case also high Cr_2O_3 ~3.00 wt% (column C). The high Al content indicates a significant solid solution with amesite component (Nelson and Roy, 1958). In an Al-Lz porphyroblast, some (001) cleavage planes are filled with barite (Fig. 3 **b**).

These considerations on the chemical composition of the three domains obtained from a number of spot analyses agree with the results of the elemental maps (App. 3, Fig. S1: Si and Mg maps), where PS of Dom 1 and Dom 2, together with lizardite and antigorite of the reaction zone, have similar serpentine compositions (grey intensity). Some large magnetite aggregates have Cr content as high as Cr_2O_3 = 12 wt% (App. 3, Fig. S1: Cr map, and Table 1). In the reaction zone, thin elongated domains of 14 Å-chlorite (App. 3, Fig. S1: Al map) and rare tiny crystals of awaruite, a Ni-Fe alloy with composition from Ni_2Fe to Ni_3Fe, and heazlewoodite, a S-poor Ni-sulphide with composition Ni_3S_2 (App. 3, Fig. S1: Ni map), are observed.

Metadunite/vein reaction zone. In the field, the PS veins are easily recognized for the ubiquitous presence at selvages of darker zones against the host metadunite (Fig. 2; App. 2, Fig. S2). The reaction zone consists of three layers with variable thickness and continuity, labelled r1, r2 and r3 (Figs. 2 **a**, **b**, **c**, **d**). In order to understand the cause of the chromatic zoning, a quantitative high-resolution X-ray elemental map (AutoPhaseMap) across the structures from the vein to the fresh metadunite (Figs. 2 **f** and **g**) was performed by SEM-EDS (App. 3, Fig. S2). The reaction front may be sharp (Fig. 6) or uneven. Despite the three bands (r1, r2, r3) observed on the altered surface of some samples (Figs. 2 **a** to **d**), the X-ray elemental map of the whole reaction zone does not show chemical zoning, but the random occurrence of a mineral assemblage

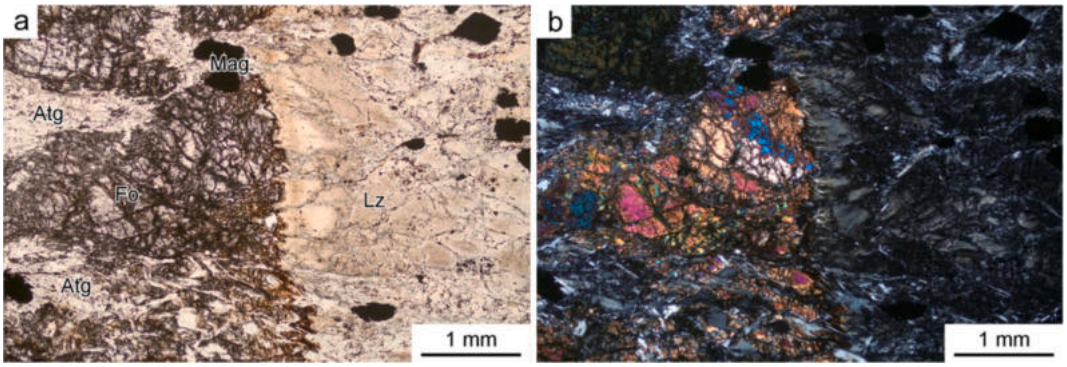

Fig. 6. Sample CF04. **a**: (PPL) and **b** (XP): Photomicrograph depicting the sharp front of the reaction zone between the PS vein (on the right, outside the picture) and the host metadunite (left) consisting of fresh forsterite (Fo) and relict antigorite (Atg) domains (grey at XP). In the reaction zone, olivine is mainly altered to light brown dusty lizardite (Lz) + very fine-grained magnetite. All black domains are magnetite (Mag). (For interpretation of the references to color in this figure legend, the reader is referred to the web version of this article.)

consisting of magnetite ± clinochlore ± brucite ± lizardite ± relict antigorite ± accessory awaruite and heazlewoodite. Other spot analyses, characterized by Mg-content higher than that of a serpentine phase, coupled with an equivalent lower Si-content, have been interpreted as a submicroscopic mixture of polygonal serpentine with brucite.

4.3. X-ray powder diffraction

The XRPD patterns of the PS veins (Table 2) were collected on Domain 2, which is the main portion of each vein and looks homogeneous under the optical microscope (cf., Figs. 2 **a**, **b** and 4 **a**, **c**). The two patterns correspond to two portions of the same vein (sample PS11) characterized by different color depth, labelled lighter and darker green, respectively. The interplanar spacings (d_{hkl}) of both patterns are similar, but the relative intensities (I/I_0) may differ, as they were obtained on rock slabs and not on rock powders. In Fig. 7, the pattern of the PS11 lighter green is compared with the diffractogram of a highly crystalline PS-30 from the literature (Barale et al., 2023; Mugnaioli et al., 2007). Both patterns show the characteristic trend of PS with the two clusters of peaks highlighted by Mugnaioli et al. (2007). Furthermore, the comparison between the two patterns indicates that the Rocciavrè veins contain both PS-15 and PS-30, with the former prevailing over the latter. PS-15 is identifiable by the presence of a series of d_{hkl} values with intensities I/I_0 greater than 10 at about 2.620, 2.500, 2.335, 2.150, 1.996 Å (Table 2, peaks highlighted in bold), and PS-30 by the strong peak at 2.450 Å (Table 2, peak highlighted in red, Fig. 7). In diffractograms of other samples, not reported in Table 2, the most intense brucite and magnetite peaks are also noted.

In conclusion, the XRPD patterns of the Rocciavrè veins confirmed the systematic association at the nanoscale of the two PS types, in agreement with TEM and μ-Raman data.

The XRPD pattern of an Al-lizardite porphyroblast, separated from the matrix and finely grinded, gave a typical diffractogram of an Al-rich lizardite (d = 7.185 Å), comparable to that studied by Brigatti et al. (1997).

4.4. Transmission electron microscopy

The TEM images were obtained from selected regions of the petrographic thin sections showing the three different domains. Overall, the three different domains consist of a felt-like mass of PS fibers, randomly oriented and associated with minor phases such as brucite and relict antigorite (Fig. 8 a, b), along with rare chrysotile (Fig. 8 **c**), in accordance with Raman results. In all three domains, both PS-15 and PS-30 were detected. The diameter of the fibers, cut perpendicular to their elongation, generally ranges from 100 to 400 nm, whereas the cross-

Table 2
Interplanar spacing (d_{hkl}) and relative intensities (I/I_0) of XRPD patterns of two representative samples (PS11 lighter and darker green) from a Rocciavrè vein that derive from central massive portions of a Dom 2. Reflections characteristic of PS-15 are in bold, whereas that typical of PS-30 is in italics. Only peaks with intensities greater than 1 were listed.

PS11 lighter green		PS11 darker green	
d_{obs}	I/I_0	d_{obs}	I/I_0
7.330	78	7.361	100
4.588	46	4.605	38
4.439	19	4.486	19
4.247	16	4.262	14
4.089	13	4.083	10
3.986	7	3.948	6
3.821	15	3.824	1
3.652	100	3.657	26
3.598	11		
3.344	4	3.342	3
3.188	4	3.188	4
3.017	1	3.030	1
2.897	7	2.908	6
2.648	14		
2.616	**17**	**2.626**	**17**
2.584	16		
2.550	11	2.557	15
2.502	**86**	**2.507**	**68**
2.453	*40*	*2.457*	*48*
2.446	29	2.431	15
2.336	**19**	**2.342**	**22**
2.278	10	2.282	8
2.209	3		
2.151	**17**	**2.156**	**15**
2.091	15	2.097	15
1.966	**17**	**1.968**	**11**
1.910	1	1.914	2
1.851	2		
1.821	3	1.828	4
1.792	3		
1.742	14	1.744	15
1.719	6		
1.639	10	1.642	6
1.602	3	1.631	5
1.536	58	1.539	50
1.503	21	1.506	20
1.461	4	1.464	5
1.417	6	1.420	6
1.384	4	1.386	4
1.323	8	1.329	3
1.310	18	1.312	18
1.278	6	1.278	5

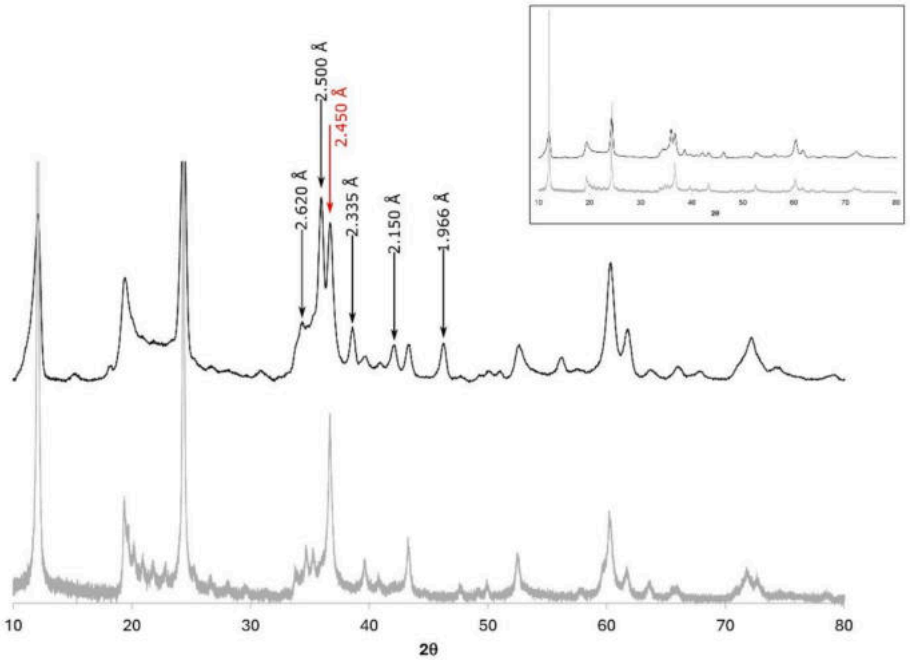

Fig. 7. Comparison between the XRPD patterns of an almost pure PS-30 with high crystallinity (grey pattern, bottom) from Mugnaioli et al. (2007) and Barale et al. (2023), and a mixed PS-15/PS-30 pattern representative of a Rocciavrè vein (black pattern, top), where the representative peaks of PS-15 are in black and the best PS-30 identifier in red. The two spectra with real intensities are shown in the box (upper right). (For interpretation of the references to color in this figure legend, the reader is referred to the web version of this article.)

section diameter of the chrysotile fibers is less than 50 nm. Brucite is abundant as discrete lamellae in Dom 3, but sporadic or even absent in Dom 1 and Dom 2. However, considering that TEM analysis samples only a small portion of the sample, we cannot exclude the presence of brucite in these domains. Moreover, brucite is present as aggregates of nanocrystals dispersed among the serpentine fibers.

TEM-EDS analyses do not show significant differences among the three domains (Table 3), except for the Fe content that increases from Dom 1 (0.74 at. %) to Dom 3 (1.03 at. %), in agreement with the SEM-EDS results (see Section 4.2). Moreover, Al and Mn, detected by SEM-EDS, were not detected at significant level by TEM-EDS. Additionally, Mg appears to be slightly higher in TEM-EDS analyses in comparison to SEM-EDS. This feature is probably a repercussion of undetected Al and Mn: being the net result normalized to 100 %, any undetected minor cation contributes to rise up the content of those detected, affecting mostly the most abundant.

A STEM-EDS map of a region of Dom 3 (Fig. 9) clearly shows sub-microscopic areas depleted in Si. Magnesium, although releasing a less clear contrast, is abundant in the Si depleted areas, suggesting the presence of brucite, which contains about one and one half more MgO than serpentine. Iron, expectedly low, releases a weak signal, which is, however, sufficient to see that Fe is unevenly distributed and appears concentrated in bands within Si poor areas. It may derive from Fe-rich brucite lamellae.

4.5. μ-Raman

Among the many μ-Raman spectra collected, the most representative associations of PS-15, PS-30 and brucite observed in several, different sites of domains 1, 2 and 3 are shown in Fig. 10. Peak assignment was based on the centroid value obtained by deconvolution, as detailed in Section 3 (Experimental methods). Although all spectra were carried out over the entire 100 to 4000 cm^{-1} range, only the high-wavenumber region (3600–3750 cm^{-1}) containing the intense OH stretching vibrations was considered.

In general, the wavenumber values of PS-15 do not differ significantly from those of PS-30, both consisting of a four-peak multiplet. Notwithstanding, the different intensities of the four peaks in the two types of polygonal serpentine yield two discriminant shapes of the resulting overall band profile: PS-15 exhibits two main peaks with that at ~3690 cm^{-1} less intense than that at ~3700 cm^{-1}, whereas PS-30 exhibits a distinctive multiplet characterized by two peaks and two shoulders with intensities progressively decreasing from 3686 cm^{-1} to 3706 cm^{-1}.

Examples 1 and 3 show similar peak shapes, consistently with a greater abundance of PS-15 relative to PS-30. This is supported by the higher intensity of peaks at ~3690 cm^{-1} and ~ 3670 cm^{-1} compared to those at ~3684 cm^{-1} and ~ 3706 cm^{-1} (Compagnoni et al., 2021). Conversely, example 2 shows a consistent progressive decrease in peak intensity from 3686 cm^{-1} to 3706 cm^{-1}, which is characteristic of PS-30 (Compagnoni et al., 2021). However, since the intensities of the PS-30 peaks can vary with crystal orientation and may overlap with PS-15 peaks, the possible presence of minor PS-15 cannot be ruled out. Possible effects of anisotropy do not invalidate the above conclusions, because the fiber orientation in the veins is random and polygonal serpentines have the lowest anisotropy among the serpentine minerals (Compagnoni et al., 2021). Additionally, the two peaks at 3645 and 3653 cm^{-1} indicate the presence of brucite, as further confirmed in the low wavelength region by two weak peaks at 279 and 445 cm^{-1}.

Overall, the results of randomly selected spot analyses from the three domains (Dom1, 2 and 3) converge with the statistically more significant Raman maps, which include over 8500 spot analyses (App. 1), indicating that, regardless of site or domain, the veins consist of sub-microscopic associations of PS-15 and/or PS-30 and/or brucite in highly variable ratios. Therefore, despite their apparent differences in hand specimen and thin section, the three domains are composed of the same mineral associations, although in highly variable ratios from point to point, as summarized in Table 4.

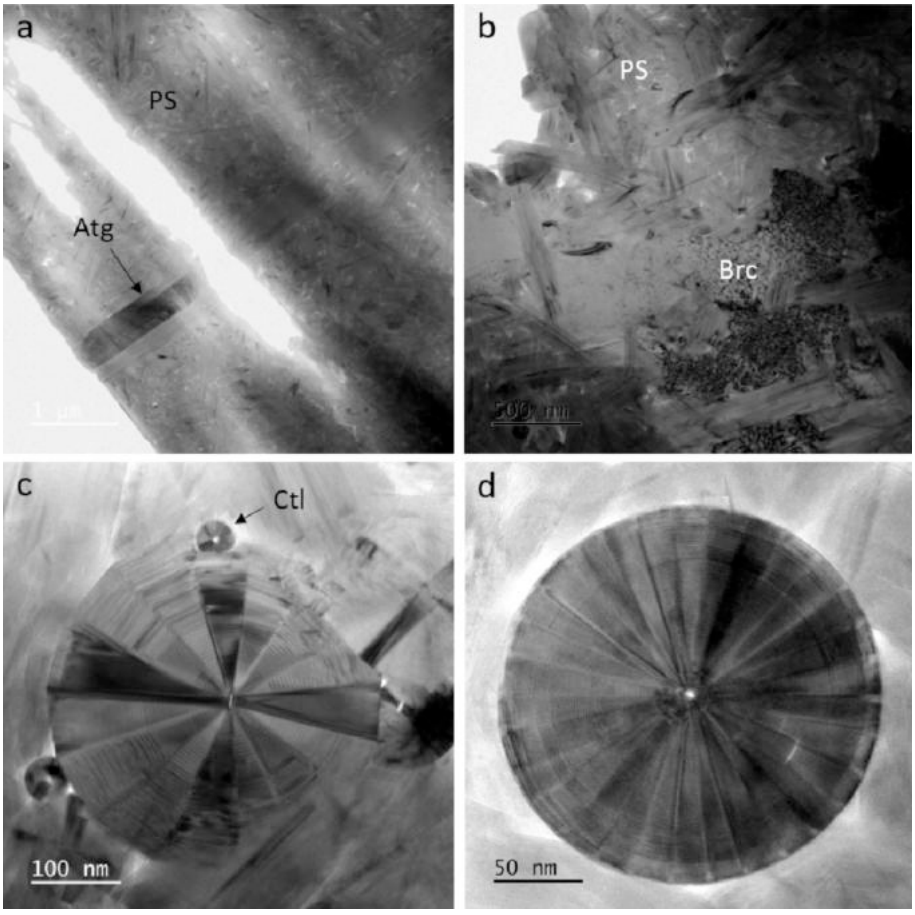

Fig. 8. Low magnification TEM bright field (BF) images of the serpentine vein of the Rocciavrè meta-ophiolite, showing a felt of randomly oriented PS fibers, together with relict antigorite (Atg) blade (**a**) and brucite (Brc) aggregates (**b**). **c**) BF image of PS-15 associated with small chrysotile (Ctl) fibers. **d**) BF image of a PS-30 fiber.

Table 3
Average TEM-EDS analyses (n. of averaged analysis in square brackets) of the three PS domains (standard deviation in brackets). a.p.f.u. are recalculated on the basis of 7 oxygens.

	Dom 1 [10]	Dom 2 [11]	Dom 3 [10]
		atom %	
O	58.22 (0.21)	58.31 (0.30)	58.19 (0.21)
Mg	24.60 (0.68)	24.11 (0.95)	24.40 (0.77)
Si	16.45 (0.42)	16.61 (0.61)	16.38 (0.41)
Fe	0.74 (0.09)	0.97 (0.15)	1.03 (0.30)
		a.p.f.u.	
Mg	2.96	2.90	2.94
Si	1.98	1.99	1.97
Fe	0.09	0.12	0.12
Σ_{Cat}	5.03	5.01	5.03

5. Discussions and conclusions

5.1. PS veins: Origin, microstructure and composition

The geological history of the Rocciavrè ultramafics is very similar to that of Monte Avic (Barale et al., 2023), because both massifs share the same tectono-metamorphic evolution. This includes: i) an early oceanic hydrothermal alteration that extensively converted the mantle peridotite to lizardite-serpentinites; ii) an early subduction phase of the Alpine orogenic cycle where Lz-serpentinites experienced a prograde HP metamorphism peaking at eclogite-facies conditions; iii) a post-collisional exhumation that only locally retrogressed the HP assemblages into greenschist- to sub-greenschist-facies conditions. A similar tectono-metamorphic evolution has also been widely described for the Voltri Massif, the most studied meta-ophiolite of the Western Alps (e.g., Barnes et al., 2014; Cannaò and Malaspina, 2018; Federico et al., 2005). The PS veins formed at the end of exhumation, when the rocks returned at the *P* and *T* conditions of the lizardite stability field.

The PS veins of the Rocciavrè meta-ophiolite appear similar to those described in the ultramafics of Monte Avic in the Aosta Valley (Barale et al., 2023), but have a more complex polyphasic history, that includes in addition to porphyroblastic Al-Lz and brucite, three different PS domains: Dom 1, Dom 2 and Dom 3. As confirmed by TEM and μ-Raman data, these three domains contain the same submicroscopic association of PS-15, PS-30 and brucite, in highly variable ratios from point to point. Like at Monte Avic, the PS veins are bounded, at the wall-rock, by two reaction zones, where olivine of metadunite is altered to an aggregate of lizardite + magnetite + brucite + minor chlorite, with accessory awaruite and heazlewoodite.

Microstructural relationships among the three domains (Dom 1, Dom 2, Dom 3) and porphyroblastic Al-Lz + brucite allowed us to reconstruct their chronological growth sequence and to attempt the reconstruction of the vein history. The polygonal habit of Dom 1 indicates that PS is pseudomorphic after a pre-existing mineral with an equant habit. Even though no relics of the original mineral have been preserved, it is reasonable to envisage it was forsterite, a phase consistent with its alteration to serpentine (± brucite) and compatible with the chemistry of the host ultramafite.

The veins are of extensional type, with simultaneous and symmetrical biaxial mineral growth (Bons, 2000, Bons et al., 2012 with refs.

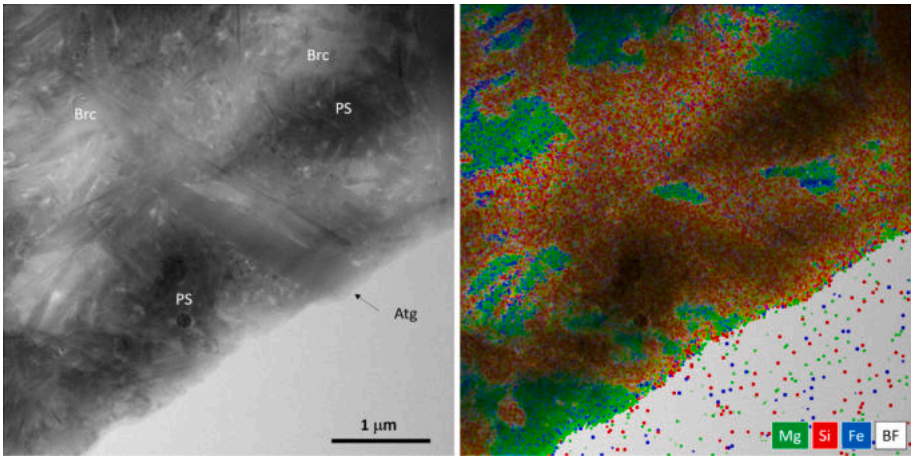

Fig. 9. BF-STEM image (left) and EDS maps (right) of Dom 3 polygonal serpentine (PS) showing areas clearly depleted in Si and slightly enriched in Mg, suggesting brucite (Brc). The Fe signal, expectedly low, appears uneven distributed, concentrated in thin bands within Si poor areas.

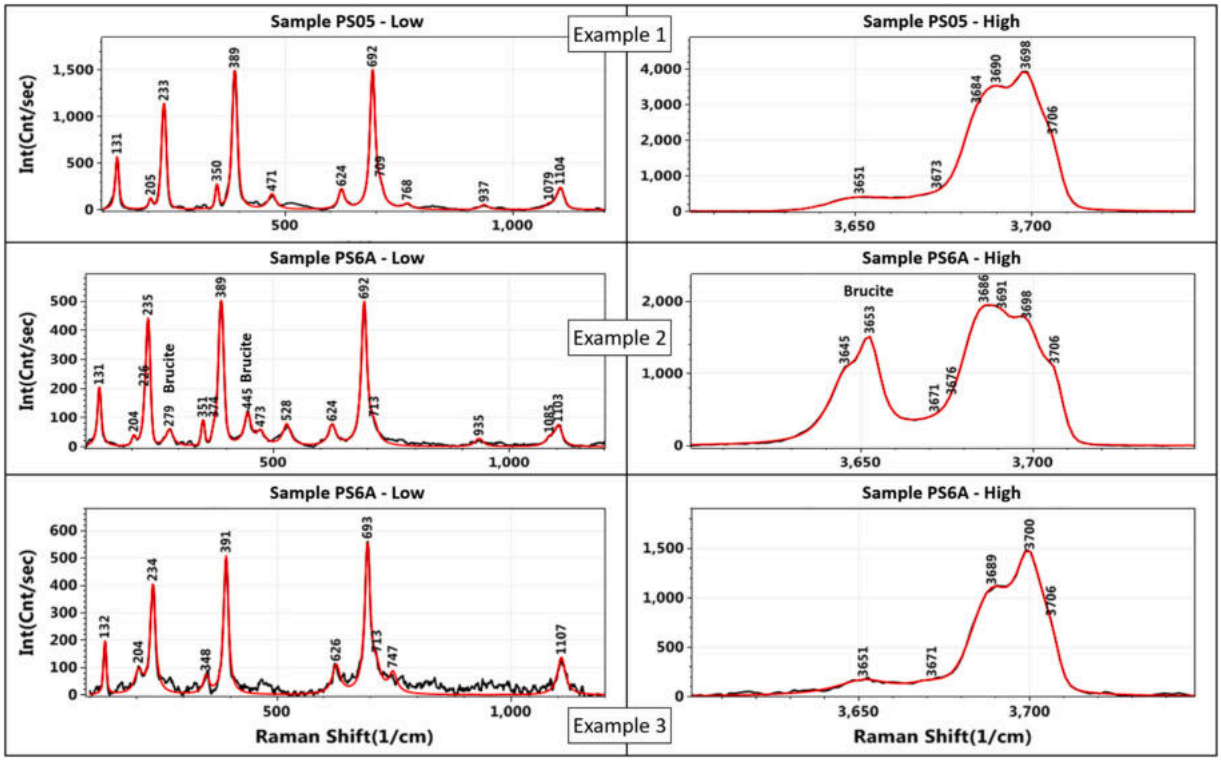

Fig. 10. Three examples of µ-Raman spectra representative of the most common associations of PS-15, PS-30 and brucite observed in different sites of domains 1, 2 and 3. The band frequencies reported refer to the centroid value obtained by deconvolution. For explanation see text.

Table 4
Mineral identification and approximate evaluation of their relative abundances as resulting from µ-Raman spot analyses summarized in the 3 examples of Fig. 10 and from the results of the µ-Raman maps (see App. 1). Symbol abbreviations: No Brc: no brucite; (R-Atg): relict antigorite from the host metadunite; PS-15(?): small amount of PS-15 is possible but not certain.

Sample	PS06b	PS07	PS10
Dom 1	PS-15 No Brc, No PS-30	PS-15 > Brc >> PS-30 (R-Atg)	PS-15 No Brc
Dom 2	PS-15 H ≈ Brc >> PS-30 (R-Atg)	PS-30 >> Brc (R-Atg)	PS-30 No Brc
Dom 3	PS-30 > Brc	PS-15 > PS-30 > Brc	PS-30 + PS-15 (?) No Brc

therein). At least four steps of dilation have been recognized: i) olivine crystals heterogeneously nucleated on the fracture walls; ii) Al-Lz and brucite porphyroblasts developed near the wall-rock, overgrowing the PS pseudomorphs after olivine; iii) aggregates of randomly oriented polygonal serpentine fibers + brucite filled the open space, sealing the vein; iv) a new generation of PS grew as radial arrays of coarser-grained fiber bundles partly replacing the PS of the third step. During the reaction process, the involved aqueous fluids were likely channelized along the original contact between wall-rock and vein.

The ubiquitous Al-Lz (and brucite) porphyroblasts developed later than forsterite, but earlier than Dom 2 being corroded and partly replaced by PS. Their peculiar "butterfly" habit suggests rapid growth in the open space of an active fracture filled with an aqueous fluid.

The main central part of the veins is made up by Dom 2, which

appears homogeneous under the polarizing optical microscope. Since Dom 2 corrodes and partially replaces Al-Lz, it is evident that the two minerals are not in equilibrium. Dom 3 is highly variable in both color and microstructure; it grows from the contact with the wall-rock (now "reaction zone") towards the vein center, forming radial fiber bundles that overgrow Dom 2 and further corrode Al-Lz. The highly variable color of Dom 3 in the thin section from pale to dark brown is interpreted as due to oxidation of Fe, higher in Dom 3 than in the other two domains.

The PS veins are crossed by late chrysotile veinlets, which are in turn cut by very thin veins consisting of euhedral brucite included in a fine-grained carbonate aggregate, identified by μ-Raman as a mixture of artinite and hydromagnesite.

The systematic intergrowth of serpentine and brucite at all scales indicates that the two minerals are in equilibrium for the reaction: Srp + H_2O = 3 Brc + 2 SiO_2, that is stable at $T < \sim 380$ °C. At a P of 1 kb (reasonable for this type of serpentinization), this assemblage is characterized by a very low silica activity, which progressively decreases from −2.5 to −3.7 (log $a SiO_2$) between 380 and 100 °C (Frost and Beard, 2007, 2008). As regards the f_{O2}, the occurrence in both PS veins and a reaction zone of awaruite (an Fe-Ni alloys) and heazlewoodite (an S-poor Ni-sulfide), suggests extremely low values for both f_{O2} and f_{S2}. In fact, as noted by Frost (1985), f_{S2} in metamorphic rocks is a function of f_{O2} because S is present dominantly as H_2S or SO_2 (rather than S_2), whose fugacities are related by the reaction: $2H_2S + 3O_2 = 2SO_2 + 2H_2O$. Sulfides are a "sensitive monitor" of f_{O2} because of the reaction: $2S_2 + 2H_2O = 2H_2S + O_2$. As f_{O2} falls, the sulfide minerals stable with magnetite become increasingly poorer in S. The low f_{O2} in the PS veins is consistent with the presence of heazlewoodite instead of millerite and pentlandite (Frost, 1985).

Finally, the very late occurrence of hydrated Mg-carbonate veins indicates that carbon dioxide entered the fluid only after the end of the serpentinization process, locally following the discontinuities previously filled by chrysotile.

5.2. P-T conditions of PS-vein formation

Since the original Dom 1 consisted of forsterite, the temperature of the mineralizing fluids must have been in the stability field of olivine, at a value around 400 °C for a pressure of 0.1 GPa (e.g., Afanasyev et al., 2014). Conversely, the PS growth in Dom 2 and Dom 3 and in the forsterite pseudomorphs after Dom 1, must have occurred in the lizardite stability field, suggesting a drop of at least 100 °C in the mineralizing fluids down to a T equal to or lower than ~300 °C (Andreani et al., 2004). At the current state of knowledge, it is impossible to constrain the low temperatures at which polygonal serpentines formed, because, similarly to chrysotile, kinetics appears to be more important than thermobaric conditions. However, the discovery in the Voltri massif of PS veins cutting across conglomerates of the ophiolitic cover (Piana et al., 2026) suggests that this uncommon type of serpentine can also form under diagenetic conditions.

5.3. Origin of the aqueous fluids

Ultramafic rocks that experienced oceanic hydrothermal alterations, during subduction to eclogite-facies conditions can release large amounts (up to 12–13 wt%) of aqueous fluids derived from the antigorite breakdown. Therefore, antigorite is commonly considered the most important source of water in subduction zones (e.g. Donoso-Tapia et al., 2025; Hattori and Guillot, 2003; Ulmer and Trommsdorff, 1995).

A recent paper by Herviou et al. (2025) on Fe-Ti metagabbros juxtaposed to the ultramafics of the Rocciavrè Massif, reports a petro-chronological study of a variety of metamorphic veins that focuses on the fluid–rock interaction processes from the early eclogite-facies subduction to the last greenschist-facies exhumation. Primary aqueous fluid inclusions trapped in both vein and host-rock minerals, characterized by intermediate to high salinity values, are interpreted "to reflect the partial signature of hydrothermal alteration preserved up to eclogite-facies conditions"; other high-salinity fluid inclusions, associated with N_2 ($\pm CO_2$) "suggest the presence of fluids produced by local dehydration reactions at peak burial". The Herviou et al. (2025) data indicate that the original hydrothermal signature acquired on the ocean floor is not erased during the complex tectono-metamorphic evolution of the whole Alpine orogenic cycle, but only partly modified by the arrival of subsequent fluids.

In the case of the PS veins, it is more difficult to trace the origin of the aqueous fluids, because serpentine minerals are unsuitable for the microthermometric study, being devoid of fluid inclusions. However, as for the Rocciavrè metagabbros studied by Herviou et al. (2025), it can be speculated that even the associated ultramafic rocks could have preserved the signature of the initial ocean-floor serpentinization. Nevertheless, it cannot be excluded that fluids of meteoric origin contributed in part or in full to the formation of the PS veins.

In this respect, Evans and coworkers, in a series of recent studies of the Troodos Ophiolite (Greece) (Evans et al., 2024a, 2024b, 2025), by means of sophisticated geochemical and isotopic analysis, such as high-resolution mapping combined with in situ boron isotope analyses and progressive leaching experiments coupled with $^{87}Sr/^{86}Sr$ signature measurements, evidenced a multistage alteration process characterized by an early serpentinization episode operated by fluids sourced from the dehydration of the subducting slab, followed by a second episode characterized by progressive recrystallisation and leaching mediated by meteoric waters.

Even though these results come from a geological context that experienced a completely different tectono-metamorphic history – the Troodos Ophiolite did not undergo an early pervasive ocean-floor hydrothermal alteration and the entire alpine collisional orogenic cycle as did the Rocciavrè Ophiolite, for instance – they substantiate that a further refinement of the current picture of the Rocciavrè Ophiolite serpentinization may come from a targeted geochemical and isotopic study.

5.4. Chrysotile vs. polygonal serpentine: Differences and similarities

Chrysotile mineralizations do not show interaction with the wall-serpentinite, as evident from the sharp vein contacts. In an exhaustive paper dealing with the chrysotile stability field, Evans (2004) concluded that the mineral is "metastable", since its "growth is favored in isotropic stress microenvironments of fluid-filled voids and pores (….) and in veins". However, chrysotile does not always form in isotropic stress microenvironments. For example, in the former mine of Balangero, the "slip" chrysotile fibers of late fracture-filling veinlets show preferred orientation parallel to direction and sense of movement along the fracture plane, where the stress is unlikely to have been isotropic (Compagnoni et al., 1980; Groppo and Compagnoni, 2007). Therefore, we believe that at least in this example, the development of chrysotile is linked more to kinetics than to energetic factors, in agreement with the results of laboratory experiments that show that synthetic chrysotile, regardless of T and P, is usually the first serpentine mineral to form and only later transforms into lizardite or antigorite, depending on the planned experimental conditions (e.g., Lafay et al., 2013; Roy and Roy, 1954; Yada and Iishi, 1974).

Unlike chrysotile, polygonal serpentine veins show clear reaction zones at the wall-rock, whose widths are roughly proportional to the vein thicknesses. This close correlation between metadunite and polygonal serpentine veins, however, does not explain why lizardite forms in the wall-rock, while polygonal serpentine in the vein. Even in this case, one could advance the explanation proposed by Evans (2004) for chrysotile, i.e. polygonal serpentine forms only in fluid-filled open fractures where stress is isotropic as well.

In a recent paper Enju et al. (2023) proposed a model in which the structure of PS results from the structure of the primitive chrysotile: orthochrysotile tends to grow into a PS-15 ortho-type and

clinochrysotile tends to grow into a PS-30 clino-type. In turn, the structure of the primitive chrysotile may depend on other factors, such as pressure: it is suggested that clinochrysotile forms at lower pressure, whereas orthochrysotile forms at high pressure. Our findings neither confirm nor deny the model proposed by Enju et al. (2023), because the poor resolution of our TEM data does not allow distinction between clino- and ortho-types. However, the occurrence of both PS-15 and PS-30 within the same domain in the same TEM mount and the fact that PS-15 is unlikely to convert to PS-30 (Baronnet and Devouard, 2005), probably suggest that pressure was not a piloting factor. Therefore, even in this case, kinetics factors seem to have played the main role.

In conclusion, the history of the Rocciavrè PS veins is very similar to, but more complex than that described at Monte Avic (Barale et al., 2023), and likewise the mineralizing fluids, must be metamorphic in origin and continental crust-derived. However, it is very unlikely that the aqueous fluids could be derived from the antigorite breakdown during subduction, because the PS veins formed at the very end of the exhumation process connected to continental collision, when the entire orogenic belt is uplifting and cooling. Conversely, since the PS veins formed at shallow depths, it is possible that the mineralizing fluids in part or entirely derived from waters of meteoric origin. A reliable answer on the origin of these fluids can only be given after a geochemical and isotopic study on these veins, which appear much more widespread than previously thought.

CRediT authorship contribution statement

Luca Barale: Investigation, Conceptualization, Resources, Writing – original draft. **Giancarlo Capitani:** Writing – review & editing, Resources, Investigation. **Roberto Compagnoni:** Writing – original draft, Investigation, Resources, Conceptualization, Resources. **Roberto Conconi:** Investigation. **Roberto Cossio:** Investigation, Writing – original draft. **Linda Pastero:** Investigation. **Marcello Mellini:** Supervision.

Declaration of competing interest

The authors declare that they have no known competing financial interests or personal relationships that could have appeared to influence the work reported in this paper.

Acknowledgements

The authors are grateful to the mineral collector Franco Manavella, who made available the first samples of veins collected in the Cassafrera depression of the Rocciavrè meta-ophiolite. Micro-Raman spectra have been obtained with the equipment acquired by the Interdepartmental Centre “G. Scansetti” for Studies on Asbestos and Other Toxic Particulates, with a grant from Compagnia di San Paolo, Torino, Italy. The PMiB has been co-funded by the Italian Ministry of University and Research (MIUR) through the “Dipartimenti di Eccellenza” 2018-2023 and 2023-2027 grants. We thank two anonymous reviewers and the editor for their helpful comments and suggestions that improved the manuscript.

Appendix A. Supplementary data

Supplementary data to this article can be found online at https://doi.org/10.1016/j.lithos.2025.108326.

References

Afanasyev, A.A., Melnik, O., Porritt, L., Schumacher, J.C., Sparks, R.S.J., 2014. Hydrothermal alteration of kimberlite by convective flows of external water. Contrib. Mineral. Petrol. 168 (1038), 1–17. https://doi.org/10.1007/s00410-014-1038-y.

Andreani, M., Baronnet, A., Bouiller, A.-M., Gratier, J.-P., 2004. A microstructural study of a “crack-seal” type serpentine vein using SEM and TEM techniques. Eur. J. Mineral. 16, 585–595. https://doi.org/10.1127/0935-1221/2004/0016-0585.

Barale, L., Capitani, G., Castello, P., Compagnoni, R., Cossio, R., Fiore, G., Pastero, L., Mellini, M., 2023. Late metamorphic veins with dominant PS-15 Polygonal Serpentine in the Monte Avic ultramafite. Eur. J. Mineral. 35, 347–360. https://doi.org/10.5194/ejm-35-347-2023.

Barnes, J.D., Beltrando, M., Lee, C.T.A., Cisneros, M., Leowy, S., Chin, E., 2014. Geochemistry of Alpine serpentinites from rifting to subduction: a view across paleogeographic domains and metamorphic grade. Chem. Geol. 389, 29–47. https://doi.org/10.1016/j.chemgeo.2014.09.012.

Baronnet, A., Devouard, B., 2005. Microstructures of common polygonal serpentines from axial HRTEM imaging, electron diffraction, and lattice-simulation data. Can. Mineral. 43, 513–542. https://doi.org/10.2113/gscanmin.43.2.513.

Baronnet, A., Mellini, M., Devouard, B., 1994. Sectors in polygonal serpentine. A model based on dislocations. Phys. Chem. Miner. 21, 330–343.

Baronnet, A., Andreani, M., Grauby, O., Devouard, B., Nitsche, S., Chaudanson, D., 2007. Onion morphology and microstructure of polyhedral serpentine. Am. Mineral. 92, 687–690. https://doi.org/10.2138/am.2007.2388.

Bons, P., 2000. The formation of veins and their microstructures. In: Jessell, Mark, Urai, Janos (Eds.), Stress, Structure and Strain: a volume in honour of Win D. Means, Journal of the Virtual Explorer, Electronic Edition, ISSN 1441-8142, volume 2, paper 4. https://doi.org/10.3809/jvirtex.2000.00007.

Bons, P.D., Elburg, M.A., Gomez-Rivas, E., 2012. A review of the formation of tectonic veins and their microstructures. J. Struct. Geol. 43, 33–62. https://doi.org/10.1016/j.jsg.2012.07.005.

Brigatti, M.F., Galli, E., Poppi, L., 1997. Crystal structure refinement of aluminian lizardite-2H_2. Am. Mineral. 82 (9–10), 931–935. https://doi.org/10.2138/am-1997-9-1010.

Cadoppi, P., Castelletto, M., Sacchi, R., Baggio, P., Carraro, F., Giraud, V., Bellardone, G., 2002. Carta Geologica d’Italia alla scala 1:50′000, Foglio 154 (Susa). Servizio Geologico d’Italia, Roma. https://hdl.handle.net/2318/1108.

Cannaò, E., Malaspina, N., 2018. From oceanic to continental subduction: implications for the geochemical and redox evolution of the supra-subduction mantle. Geosphere 14, 2311–2336. https://doi.org/10.1130/GES01597.1.

Capitani, G., Mellini, M., 2004. The modulated crystal structure of antigorite: the $m = 17$ polysome. Am. Mineral. 89 (1), 147–158. https://doi.org/10.2138/am-2004-0117.

Capitani, G., Mellini, M., 2006. The crystal structure of a second antigorite polysome ($m = 16$), by single-crystal synchrotron diffraction. Am. Mineral. 91 (2–3), 394–399. https://doi.org/10.2138/am.2006.1919.

Compagnoni, R., Sandrone, R., Zucchetti, S., 1980. Some remarks on the asbestos occurrences in the Western Alps, with special reference to the chrysotile asbestos deposit of Balangero (Lanzo Valley, Piedmont, Italy). 4th Intern. Conf. On Asbestos, Torino (Italy), 26-30 May 1980. Pre-prints 1, 49–71.

Compagnoni, R., Cossio, R., Mellini, M., 2021. Raman anisotropy in serpentine minerals, with a caveat on identification. J. Raman Spectrosc. 52, 1334–1345. https://doi.org/10.1002/jrs.6128.

Conconi, R., Ventruti, G., Nieto, F., Capitani, G., 2023. TEM-EDS microanalysis: Comparison among the standardless, Cliff & Lorimer and absorption correction quantification methods. Ultramicroscopy 254, 113845. https://doi.org/10.1016/j.ultramafic.2023.113845.

Cressey, G., Cressey, B.A., Wicks, F.J., 2008. Polyhedral serpentine: a spherical analogue of polygonal serpentine? Mineral. Mag. 72, 1229–1242. https://doi.org/10.1180/minmag.2008.072.6.1229.

Donoso-Tapia, D., Flores, K.E., Celine, M., Hull, S., Hernández-Uribe, D., Gazel, E., 2025. Record of de-serpentinization and re-serpentinization of an exhumed slab sliver: Implications for fluid circulation in subduction zones. Earth Planet. Sci. Lett. 653, 119213. https://doi.org/10.1016/j.epsl.2025.119213.

Enju, S., Uehara, S., Inoo, T., 2023. Polygonal Serpentine and Chrysotile in the Kurosegawa Belt, Kyushu, Japan. Can. J. Mineral. Petrol. 61, 145–166. https://doi.org/10.3749/2200017.

Evans, A.D., Craw, D., Teagle, D.A.H., 2024a. Active near-surface mobilisation of slab-derived geochemical signatures by hyperalkaline waters in brecciated serpentinites. Chem. Geol. 643, 121822. https://doi.org/10.1016/j.chemgeo.2023.121822.

Evans, A.D., Cooper, M.J., Craw, D., Teagle, D.A.H., 2025. Multiple episodes of serpentinite alteration revealed by progressive leaching experiments. Geochim. Cosmochim. Acta 397, 188–204. https://doi.org/10.1016/j.gca.2025.04.001.

Evans, A.E., Standish, C.D., Milton, J.A., Robbins, A.G., Craw, D., Foster, G.L., Teagle, D.A.H., 2024b. Imaging of boron in altered mantle rocks illuminates progressive serpentinisation episodes. Geochem. Persp. Let. 29, 20–25. https://doi.org/10.7185/geochemlet.2407.

Evans, B.W., 2004. The serpentinite multisystem revisited: chrysotile is metastable. Int. Geol. Rev. 46, 479–506. https://doi.org/10.2747/0020-6814.46.6.479.

Federico, L., Capponi, G., Crispini, L., Scambelluri, M., Villa, I.M., 2005. 39Ar/40Ar dating of high-pressure rocks from the Ligurian Alps: evidence for a continuous subduction exhumation cycle: Earth Planet. Sci. Lett. 240 (3–4), 668–680. https://doi.org/10.1016/j.epsl.2005.09.062.

Frost, B.R., 1985. On the stability of sulfides, oxides, and native metals in serpentinite. J. Petrol. 26 (1), 31–63. https://doi.org/10.1093/petrology/26.1.31.

Frost, B.R., Beard, J.S., 2007. On Silica activity and Serpentinization. J. Petrol. 48 (7), 1351–1368. https://doi.org/10.1029/2024GL114016.

Frost, B.R., Beard, J.S., 2008. On Silica activity and Serpentinization: Errata. J. Petrol. 49 (6), 1253.

Groppo, C., Compagnoni, R., 2007. Metamorphic veins from the serpentinites of the Piemonte Zone, western Alps, Italy: a review. Period. Mineral. 76, 127–153. https://doi.org/10.2451/2007PM0021.

Hattori, K.H., Guillot, S., 2003. Volcanic fronts form as a consequence of serpentinite dehydration in the forearc mantle wedge. Geology 31 (6), 525–528. https://doi.org/10.1130/0091-7613(2003)031<0525:VFFAAC>2.0.CO;2.

Herviou, C., Bonnet, G., Angiboust, S., Cambeses, A., Raimondo, T., 2025. Petrochronology of high-pressure veins reveals the evolution of fluid sources in subducted oceanic crust (Rocciavrè Eclogites, W. Alps). J. Metamorph. Geol. 43, 225–256. https://doi.org/10.1111/jmg.12806.

Lafay, R., Montes-Hernandez, G., Janots, E., Chiriac, R., Findling, N., Toche, F., 2013. Nucleation and growth of chrysotile nanotubes in H_2SiO_3/$MgCl_2$/NaOH medium at 90 to 300 °C. Chem. Eur. J. 19 (17), 5417–5424. https://doi.org/10.1002/chem.201204105.

Lanari, P.O., De Andrade, V., Dubacq, B., Lewin, E., Eugene, G., Grosch, E.G., Schwartz, S., 2014. XMapTools: a MATLAB©-based program for electron microprobe X-ray image processing and geothermobarometry. Comput. Geosci. 62, 227–240. https://doi.org/10.1016/j.cageo.2013.08.010.

Manavella, F., Salusso, F., Magrì, F., Costa, E., 2021. Awaruite e heazlewoodite nelle serpentiniti di Località Cassafrera (Rocciavrè), Alpi Cozie, Piemonte sud-occidentale. Micro 19 (3), 164–173 (in Italian).

Mellini, M., 1982. The crystal structure of lizardite 1T: hydrogen bonds and polytypism. Am. Mineral. 67, 587–598. https://pubs.geoscienceworld.org/msa/ammin/article-abstract/67/5-6/587/41395/The-crystal-structure-of-lizardite-1T-hydrogen.

Mellini, M., 1986. Chrysotile and polygonal serpentine from the Balangero serpentinite. Mineral. Mag. 50, 301–305. https://doi.org/10.1180/minmag.1986.050.356.17.

Mugnaioli, E., Logar, M., Mellini, M., Viti, C., 2007. Complexity in 15- and 30-sectors polygonal serpentine: Longitudinal sections, intrasector stacking faults and XRPD satellites. Am. Mineral. 92, 603–616. https://doi.org/10.2138/am.2007.2272.

Nelson, B.W., Roy, R., 1958. Synthesis of the chlorites and their structural and chemical constitution. Am. Mineral. 42, 707–725. https://pubs.geoscienceworld.org/msa/ammin/article-abstract/43/7-8/707/541385/Synthesis-of-the-chlorites-and-their-structural.

Piana, F., Barale, L., Compagnoni, R., d'Atri, A., Fioraso, G., Irace, A., Mosca, P., Tallone, S., Monegato, G., Morelli, M., 2017. Geological map of piemonte region at 1: 250,000 scale. Explanatory notes. Accademia Scienze Torino, Memorie Scienze Fisiche 41, 3–143. https://hdl.handle.net/2318/1715491.

Piana, F., Barale, L., d'Atri, A., Irace, A., Mantovani, A., Marcelli, I., Mosca, P., Ossella, L., Bertok, C., Frasca, G., Catanzariti, R., 2026. Note Illustrative dela Carta Geologica d'Italia alla scala 1:50.000 – Foglio 195 Novi Ligure. In: ISPRA – Servizio Geologico d'Italia, Roma.

Pognante, U., 1979. The Orsiera-Rocciavrè metaophiolitic complex (Italian Western Alps). Ofioliti 4 (2), 183–198.

Pognante, U., 1985. Coronitic Reactions and Ductile Shear zones in Eclogitised Ophiolite Metagabbro, Western Alps, North Italy. Chem. Geol. 50, 99–109. https://doi.org/10.1016/0009-2541(85)90114-7.

Roy, D.M., Roy, R., 1954. An experimental study of the formation and properties of synthetic serpentines and related layer silicate minerals. Am. Mineral. 39 (11−12), 957–975.

Ulmer, P., Trommsdorff, V., 1995. Serpentine Stability to Mantle Depths and Subduction-Related Magmatism. Science 268, 858–861. https://doi.org/10.1126/science.268.5212.858.

Whittaker, E.J.W., Zussman, J., 1956. The characterization of serpentine minerals by X-ray diffraction. Mineral. Mag. 233, 107–126. https://doi.org/10.1180/minmag.1956.031.233.01.

Wojdyr, M., 2010. Fityk: a general-purpose peak fitting program. J. Appl. Crystallogr. 43, 1126–1128. https://doi.org/10.1107/S0021889810030499.

Yada, K., Iishi, K., 1974. Serpentine minerals hydrothermally synthesized and their microstructures. J. Cryst. Growth 24 (25), 627–630.